

Dual-Decoder Consistency via Pseudo-Labels Guided Data Augmentation for Semi-Supervised Medical Image Segmentation

Yuanbin Chen, Tao Wang, Hui Tang, Longxuan Zhao, Ruige Zong, Tao Tan, Xinlin Zhang, and Tong Tong

Abstract—Medical image segmentation methods often rely on fully supervised approaches to achieve excellent performance, which is contingent upon having an extensive set of labeled images for training. However, annotating medical images is both expensive and time-consuming. Semi-supervised learning offers a solution by leveraging numerous unlabeled images alongside a limited set of annotated ones. In this paper, we introduce a semi-supervised medical image segmentation method based on the mean-teacher model, referred to as Dual-Decoder Consistency via Pseudo-Labels Guided Data Augmentation (DCPA). This method combines consistency regularization, pseudo-labels, and data augmentation to enhance the efficacy of semi-supervised segmentation. Firstly, the proposed model comprises both student and teacher models with a shared encoder and two distinct decoders employing different up-sampling strategies. Minimizing the output discrepancy between decoders enforces the generation of consistent representations, serving as regularization during student model training. Secondly, we introduce mixup operations to blend unlabeled data with labeled data, creating mixed data and thereby achieving data augmentation. Lastly, pseudo-labels are generated by the teacher model and utilized as labels for mixed data to compute unsupervised loss. We compare the segmentation results of the DCPA model with six state-of-the-art semi-supervised methods on three publicly available medical datasets. Beyond classical 10% and 20% semi-supervised settings, we investigate performance with less supervision (5% labeled data). Experimental outcomes demonstrate that our approach consistently outperforms existing semi-supervised medical image segmentation methods across the three semi-supervised settings.

Index Terms—Semi-supervised learning, medical image segmentation, consistency, pseudo-labels, data augmentation.

I. INTRODUCTION

This work was supported by National Natural Science Foundation of China under Grant 62171133, in part by the Artificial Intelligence and Economy Integration Platform of Fujian Province, and the Fujian Health Commission under Grant 2022ZD01003. (Corresponding author: Xinlin Zhang, Tong Tong.)

This work was supported by National Natural Science Foundation of China under Grant 62171133, in part by the Artificial Intelligence and Economy Integration Platform of Fujian Province, and the Fujian Health Commission under Grant 2022ZD01003. (Corresponding author: Xinlin Zhang, Tong Tong.)

Yuanbin Chen, Tao Wang, Hui Tang, Longxuan Zhao, Ruige Zong, Xinlin Zhang, TongTong are with the College of Physics and Information Engineering, Fuzhou University, Fuzhou 350116, China, and also with the Fujian Key Lab of Medical Instrumentation & Pharmaceutical Technology, Fuzhou University, Fuzhou 350116, China (e-mail: binycn904363330@gmail.com, ortonwangtao@gmail.com, yeaahelana@gmail.com, zlx1154692412@gmail.com, zongruige@gmail.com, xinlin1219@gmail.com, ttravelong@gmail.com).

Tao Tan is with the Department of the Faculty of Applied Science, Macao Polytechnic University, Macao, 999078, China (e-mail: taotansj@gmail.com).

IN the field of medical image analysis, image segmentation holds a crucial and indispensable role, especially when it comes to delineating internal structures within medical images such as computerized tomography (CT) or magnetic resonance imaging (MRI) scans to address clinical requirements. Deep learning has witnessed remarkable advancements, wherein convolutional neural networks (CNNs) have showcased cutting-edge performance across various automated image segmentation tasks. Prominent methodologies, such as fully convolutional networks (FCNs) [1] and encoder-decoder networks (e.g., U-Net [2] and V-Net [3]), have been extensively adopted for diverse medical image segmentation endeavors. The success of these approaches can be attributed to the availability of meticulously annotated datasets that exhibit exceptional quality. However, obtaining annotations for medical images presents considerable financial and labor-intensive challenges, primarily due to the expertise and time required for accurate delineation, especially when manually annotating medical images at the pixel/voxel level, as seen in volume CT or MRI scans. To address the annotation burden in medical image segmentation while upholding high accuracy in the resultant segmentations, semi-supervised learning methods have emerged as a viable solution. These approaches effectively diminish the dependence on medical image annotations by leveraging a limited set of labeled data alongside an extensive pool of unlabeled data, thereby demonstrating widespread applicability in the domain of medical image segmentation tasks [4].

Semi-supervised learning aims to achieve effective learning outcomes by synergistically integrating a limited quantity of labeled data with a substantial volume of unlabeled data. Within the realm of semi-supervised learning, the formulation of effective strategies for supervising unlabeled data assumes paramount significance, giving rise to the emergence of diverse approaches that adeptly exploit the latent potential of unlabeled images. Currently, semi-supervised methods can be primarily classified into three distinct categories: (1) Consistency regularization methods [5]–[7], which induce the model to exhibit consistent output distributions when subjected to input perturbations. By subjecting the unlabeled data to diverse perturbations or employing augmentation techniques, the model is compelled to generate coherent predictions, thereby augmenting its generalization capability. (2) Entropy minimization methods [8]–[10], which are grounded in the clustering assumption, actively encourage the model to make confident predictions on unlabeled data. Through the min-

imization of entropy in the predicted probability distribution, the model acquires an increased degree of certainty, consequently fortifying its learning effectiveness. (3) Pseudo-labeling methods [11]–[13], serving as a mechanism to enrich the training set, enhance model performance by generating pseudo-labels from the unlabeled data.

Although semi-supervised learning methods have achieved success in medical image segmentation, they still face challenges. Selecting appropriate methods and designing effective regularization techniques are crucial tasks due to different methods’ advantages and limitations. The imbalance between labeled and unlabeled data can affect the performance of semi-supervised learning methods. The availability of a large amount of unlabeled data may cause imbalance during the learning process, biasing models towards unlabeled data. Additionally, medical image data exhibit complex and diverse characteristics, such as variations in imaging modalities, noise, and anatomical differences. These factors pose challenges for semi-supervised learning methods as they may struggle to capture underlying patterns and generalize well across different datasets. Therefore, addressing these issues and developing robust semi-supervised learning methods remains an important research direction.

To address the challenges mentioned above, this paper introduces a novel semi-supervised medical image segmentation approach called Dual-Decoder Consistency via Pseudo-Label Guided Data Augmentation (DCPA) based on the mean-teacher model [6]. The primary objective of DCPA is to enhance the utilization of unlabeled regions by employing pseudo-label guided data augmentation and extracting more informative features from the unlabeled data through dual-decoder consistency. Specifically, the DCPA model comprises both teacher and a student models with a shared encoder and dual-decoder with distinct strategies. The teacher model generates pseudo-labels for the unlabeled data. Subsequently, data augmentation is performed by blending the unlabeled data with the labeled data using Mixup [14], where the pseudo-labels serve as the labels for the mixed data. Finally, the output discrepancies between the decoders of the student model are minimized through consistency constraints. The significant contributions of this study are as follows:

- We propose a novel semi-supervised medical image segmentation approach based on pseudo-labels and consistency. The fundamental concept is to utilize pseudo-labels guided data augmentation and enforce consistency constraints on the model’s predictions. This approach effectively leverages the information from the unlabeled data, leading to enhanced performance in the context of semi-supervised image segmentation.
- We have devised a dual-decoder network based on the mean teacher model and employed a consistency scheme to constrain the model’s training process, enabling it to acquire generalized feature representations.
- We extensively validated the proposed method on three challenging public medical image segmentation tasks. The extensive experimental results conclusively demonstrate that the proposed DCPA model outperforms the six most recent methods and establishes a new state-of-the-art for semi-

supervised medical image segmentation.

II. RELATED WORK

A. Medical image segmentation

In recent years, deep learning methods have been extensively applied in the domains of computer vision and medical image analysis. Particularly in the field of medical image segmentation, the utilization of encoder-decoder architectures based on FCNs [1], such as UNet [2] and nnUNet [15], has significantly advanced the accuracy of various modalities and segmentation tasks. These extension methods primarily focus on enhancing performance through data augmentation, improving network architectures, and designing effective loss functions. Data augmentation, a simple yet effective technique, has been empirically demonstrated to play a crucial role in enhancing model performance and robustness, as supported by recent studies [16]. Mixup [14] is a straightforward yet powerful data augmentation technique that enriches the diversity of the dataset and enhances the model’s robustness and generalization capabilities through the generation of interpolated samples. The selection of an appropriate network architecture is paramount for deep learning-based medical image segmentation algorithms. Current research primarily revolves around integrating novel modules, including attention mechanisms, residual blocks, and pyramid fusion modules, with the UNet [2] framework to demonstrate superior performance. For instance, AG-Net [17] incorporates an attention gate module before skip connections to better preserve structural information. Res-Unet [18] introduces residual connections [19] into the UNet structure, thereby improving gradient flow, preventing network degradation, and expediting convergence. CE-Net [20] proposes a DAC module and an RMP module to capture more advanced features and retain additional spatial information. Moreover, the application of Transformer models [21] has garnered significant attention in the field of medical image segmentation due to their exceptional capacity for modeling global context. Swin-Unet [22] employs a layered Swin Transformer [23] with shifted windows as an encoder, enabling the extraction of contextual features. Additionally, it designs a symmetric decoder with patch expansion layers based on the Swin Transformer [23] for performing upsampling operations, thereby restoring the spatial resolution of feature maps. Loss functions play an indispensable role in model training, aiming to minimize the discrepancy between network predictions and true labels. These loss functions can be categorized into three types: (1) distribution-based losses, such as cross-entropy loss [2], which aim to maximize the similarity between predictions and true labels in the distribution space; (2) region-based losses, such as Dice loss [3], which strive to minimize the discrepancy between predictions and true labels; (3) distance-based losses, such as boundary loss [24], which aim to minimize the boundary distance between predictions and true labels in Euclidean distance space.

B. Semi-supervised learning

Semi-supervised learning is a significant machine learning approach that integrates the characteristics of unsupervised

and supervised learning [25]. Its primary objective is to effectively leverage a limited amount of labeled data and a substantial quantity of unlabeled data for model training and prediction. Semi-supervised learning has demonstrated wide-ranging applications in domains such as natural language processing and computer vision. Among the numerous methods employed in semi-supervised learning, one prominent approach is consistency regularization, which is grounded in the assumptions of clustering and smoothness. In this context, Laine et al. [5] proposed a technique that promotes consistent predictions on unlabeled data by minimizing the consistency loss, resulting in a noteworthy enhancement in the overall performance of semi-supervised learning. Another notable method is the mean-teacher model introduced by Tarvainen et al. [6], consisting of a student model and a teacher model with shared architecture. By employing the Exponential Moving Average (EMA) technique, the authors successfully integrated past parameters, thereby reducing discrepancies between the models. Within the teacher-student framework, Zhao et al. [26] addressed the issue of student models suppressing teacher models during the training phase. They presented a novel solution by substituting the classical EMA algorithm with a stable voxel-based information exchange paradigm, effectively resolving this problem. Entropy minimization, grounded in information theory, is another widely utilized approach in semi-supervised learning [27]. Berthelot et al. [9] astutely combined consistency regularization and entropy minimization methods, leveraging both labeled and unlabeled samples to learn more robust and consistent feature representations from unlabeled data, thereby enhancing the model’s generalization capability. Additionally, the utilization of pseudo-labels provides supplementary training signals derived from unlabeled data, further augmenting the overall model performance. Rizve et al. [12] unified probability and uncertainty thresholds to ascertain the most accurate pseudo-labels. These advancements in pseudo-labels selection, in conjunction with consistency regularization, entropy minimization, and other techniques, have achieved state-of-the-art performance on diverse benchmark datasets.

C. Semi-supervised medical image segmentation

In recent years, semi-supervised medical image segmentation has received considerable attention as a means to alleviate the burden of manual labeling, leading to the development of various methods. Consistency regularization has emerged as a prominent technique in this field. Yu et al. [28] proposed an uncertainty-aware mean-teacher model to segment the left atrium, leveraging uncertainty maps to guide the incremental learning process using unlabeled data. TCSM-V2 [29] introduced additional data and model perturbations, such as flipping, rotation, resizing, adding noise, and dropout, within the mean-teacher framework [6] to establish consistency in model predictions across different perturbations of the same input. Another research direction in consistency regularization involves the use of multi-task level consistency constraints. Li et al. [30] employed a commonly used multi-task network structure for image segmentation and signed distance

map regression, incorporating shape and position priors. They employed a discriminator as a regularization term to ensure stability and robustness of the segmentation results. Luo et al. [31] explored consistency based on representation differences between tasks, focusing on organ shape regression. They proposed an uncertainty-corrected pyramid consistency that leverages multi-level features in the network [32], enforcing consistency loss and incorporating uncertainty-corrected predictions. Wang et al. [33] achieved semantic data augmentation by utilizing semantic directions in the feature space and further improved model performance through the application of consistency constraints in semi-supervised learning. Entropy minimization is another technique that enhances the confidence of network predictions. Hang et al. [33] introduced entropy minimization into the student network, generating highly confident predictions for unlabeled images. They designed a local structure consistency loss that encourages consistency between voxels in the same local region of the teacher and student networks. Moreover, they achieved global structure consistency by matching the weighted self-information mapping between the two networks. Recognizing the effectiveness of consistency regularization and entropy minimization in utilizing unlabeled data, Wu et al. [34] proposed a novel training strategy called Mutual Consistency Learning, significantly improving the performance of semi-supervised learning by applying these two constraints during the training process. Additionally, the use of pseudo-labels is a common approach in semi-supervised medical image segmentation. Wang et al. [35] suggested incorporating a trust module to re-evaluate the pseudo-labels obtained from model outputs, establishing a threshold to select high-confidence values. Li et al. [36] introduced a self-ensembling strategy that utilizes EMA to generate accurate and reliable predictions, addressing issues associated with noisy and unstable pseudo-labels.

III. METHOD

In order to present a concise and accurate depiction of our research, we first introduce some fundamental equations of semi-supervised learning prior to introducing our proposed model. The training data set is divided into two distinct subsets: a labeled data set denoted as D_L^N , comprising N samples, and an unlabeled data set denoted as D_U^M , comprising M samples. It is assumed that for an image $x_i \in D_L^N$, its corresponding ground truth label y_i is provided, whereas for an image $x_i \in D_U^M$, the ground truth label is unavailable. Consequently, the two data sets can be formally represented as $D_L^N = \{x_i^i, y_i^i | i \in (1, \dots, N)\}$ and $D_U^M = \{x_u^i | i \in (1, \dots, M)\}$. $p(y_{pred}|x; \theta)$ represents the generated probability map of x , where θ denotes the parameters of the segmentation model $f(\theta)$.

A. Model architecture

In this paper, we propose a novel semi-supervised medical image segmentation method called DCPA. As depicted in Fig. 1, the DCPA framework consists of two fundamental components. Firstly, we leverage unlabeled data to generate pseudo-labels and employ Mixup to effectively perform data

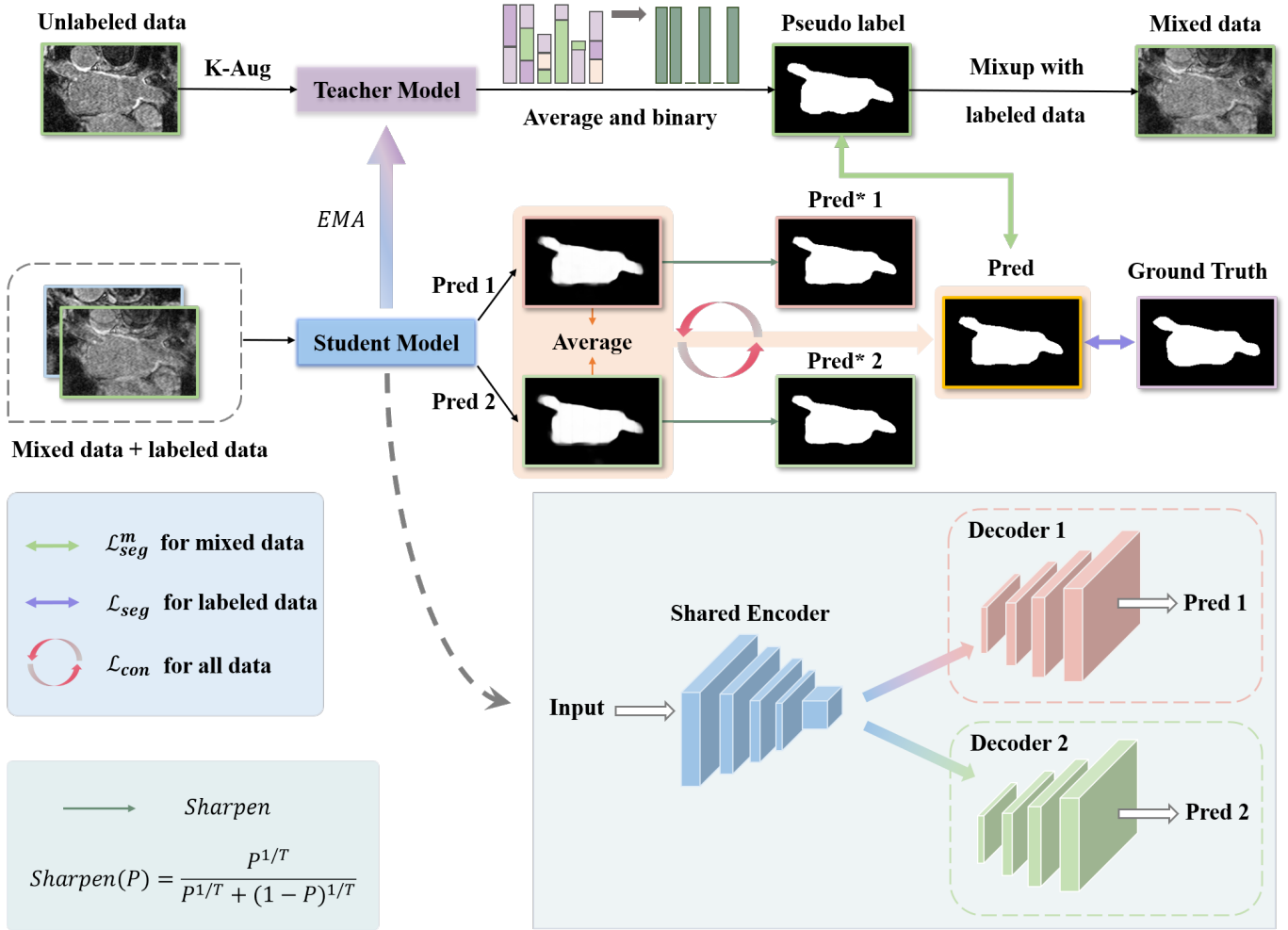


Fig. 1. Overview of the proposed DCPA method. Detailed descriptions of both the teacher model and the student model are provided beneath the figure. Notably, Decoder 1 and Decoder 2 correspond to two distinct decoders employing different upsampling strategies. The circular annotations of L_{con} indicate the computation of consistency loss between Pred 1 and Pred* 2, as well as between Pred 2 and Pred* 1.

augmentation by combining unlabeled data with labeled data. Subsequently, the augmented data is utilized for training the student model. It is essential to highlight that the proposed student and teacher models share a unified architecture, comprising a shared encoder and dual-decoder with distinct upsampling strategies. The primary distinction lies in the training process, where the student model is trained using a specific loss function, while the teacher model applies EMA to the weights of the student model. Further detailed explanations of these aspects will be provided in subsequent sections.

B. Generating Pseudo-Labels

To begin with, we employ weak data augmentation (e.g., random perturbations) on both labeled and unlabeled images. For each batch of labeled images $X_L^b \in D_L^N$, we produce a transformed version $\hat{X}_L^b = \text{Aug}(X_L^b)$. Different from labeled data, for each batch of unlabeled images $X_U^b \in D_U^M$, we produce K transformed version $\hat{X}_U^{b,k} = \text{Augment}(X_U^b, k) \in (1, \dots, K)$. Subsequently, we utilize the teacher model to obtain the average predicted segmentation distribution \bar{P}^b from the augmented unlabeled samples. Finally, we apply a binary

operation to \bar{P}^b to obtain the pseudo-labels P^b . The specific computation formulas are as follows:

$$\bar{P}^b = \frac{1}{K} \sum_{k=1}^K p(y_{pred} | \hat{X}_U^{b,k}; \theta_t), \quad (1)$$

$$P^b(x, y) = \begin{cases} 1, & \text{if } \bar{P}^b(x, y) \geq H, \\ 0, & \text{otherwise.} \end{cases} \quad (2)$$

Where θ_t denotes the parameters of the teacher model. $P^b(x, y)$ represents the pixel value at coordinate (x, y) in the pseudo-labels. The threshold H (usually set to 0.5 in most cases) is used to determine whether a pixel should be assigned the value 1 in the pseudo-labels. If the pixel value in \bar{P}^b is greater than or equal to the threshold H , the corresponding pixel value in the pseudo-labels P^b is set to 1; otherwise, it is set to 0. The obtained pseudo-labels P^b is subsequently used for the unsupervised loss term.

C. Pseudo-Labels Guided Data Augmentation

Inspired by Mixmatch [9], we utilize MixUp [14] to blend the augmented unlabeled images with the augmented labeled

images, thereby enhancing the richness of the data through data augmentation. For a pair of two images x_1, x_2 , the mixed images x' is defined as:

$$\lambda \sim \text{Random}(\text{Beta}(\alpha, \alpha)), \quad (3)$$

$$\lambda' = \text{Max}(\lambda, 1 - \lambda), \quad (4)$$

$$x' = \lambda' x_1 + (1 - \lambda') x_2, \quad (5)$$

Where α is a hyperparameter. In contrast to Mixmatch [9], we refrain from employing the MixUp [14] on the labeled images. This decision arises from the intricate nature of medical images, characterized by substantial variations in morphology, size, and position of structures. Therefore, our approach exclusively applies the MixUp operation to the unlabeled images.

Fig. 2 illustrates the results of applying Mixup [14] to two images. It can be observed that after Mixup, the mixed image is predominantly influenced by the semantic information of the unlabeled data. However, due to the involvement of labeled data, some changes occur in the image, particularly in the region enclosed by the red rectangle. Nevertheless, these changes do not significantly alter the overall semantic information of the image. Hence, we opt to use the pseudo-labels P^b as the label for the mixed image. To facilitate the application of MixUp, we commence by shuffling the augmented labeled images \hat{X}_L^b to establish set W^b . Following this, we apply the MixUp to combine the augmented unlabeled images $\hat{X}_U^{b,k}$ with set W^b , ultimately giving rise to the formation of mixed images $M^{b,k}$. Finally, the obtained mixed images are combined with pseudo-labels P^b to generate mixed data D_M . The specific formulas are as follows:

$$W^b = \text{Shuffle}(\hat{X}_L^b), \quad (6)$$

$$M^{b,k} = \left(\text{Mixup}(\hat{X}_U^{b,k}, W_{i\%|\hat{X}_L^b|}^b); i \in (1, \dots, |\hat{X}_U^{b,k}|) \right), \quad (7)$$

$$D_M = ((M^{b,k}, P^b); b \in (1, \dots, B), k \in (1, \dots, K)), \quad (8)$$

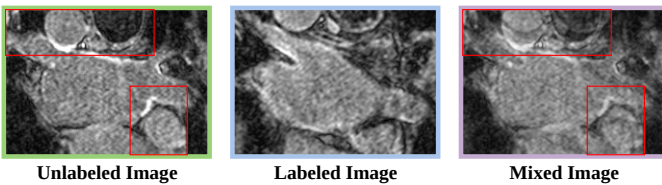


Fig. 2. Illustration showcasing the effects of Mixup. The red rectangles within the image highlight areas where noticeable alterations are observed before and after applying Mixup.

D. Dual-Decoder Consistency

In Fig. 1, we present the architecture of the student and teacher models, where the VNet is utilized as the underlying backbone, comprising a shared encoder and dual-decoder with distinct strategies, namely the transposed convolutional layer and the linear interpolation layer. This design leverages the differences between the decoder outputs to capture and represent the model’s uncertainty information. To improve the quality of the pseudo-labels generated from the unlabeled data, the teacher model’s parameters are accumulated using the Exponential Moving Average (EMA) of the student model’s parameters, facilitating the integration of historical states during the learning process. The effectiveness of this approach has been validated in [6]. The update rule for the teacher model’s parameters at the current time step, denoted as θ'_t , is defined as:

$$\theta'_t = \alpha \theta'_t - 1 + (1 - \alpha) \theta_t, \quad (9)$$

Where $\theta'_t - 1$ represents the historical parameters of the teacher model, while θ_t represents the parameters of the student model at the current time step. The hyperparameter α serves as a smoothing coefficient, determining the interdependence between the teacher and student models. Building upon the previously obtained D_M , we feed the input $x \in D_L^N \cup D_M$ through the student model to derive $Pred_1 = p(y_{pred_1} | x; \theta_s)$ and $Pred_2 = p(y_{pred_2} | x; \theta_s)$, where θ_s denotes the student model’s parameters. To effectively leverage the unlabeled data, considering the benefits of both consistency constraint and entropy minimization, we employ a sharpening function to reduce the entropy of the probability maps generated by the student model. This process yields soft-pseudo-labels $Pred_i^*$ formulated as:

$$Pred_i^* = \frac{Pred_i^{\frac{1}{T}}}{Pred_i^{\frac{1}{T}} + (1 - Pred_i)^{\frac{1}{T}}}, i \in (1, 2), \quad (10)$$

Where T is a hyperparameter used to control the sharpening temperature. As $T \rightarrow 0$, the output of $Pred_i^*$ approaches a Dirac (“one-hot”) distribution. Thus, to enhance the constraint of entropy minimization, we decrease the temperature to encourage the model to generate predictions with lower entropy. Fig. 3 demonstrates that the application of the sharpening operation enhances the clarity and details of the segmentation boundaries, while reducing the presence of blurry features in the image, especially in the region marked by the red boxed area.

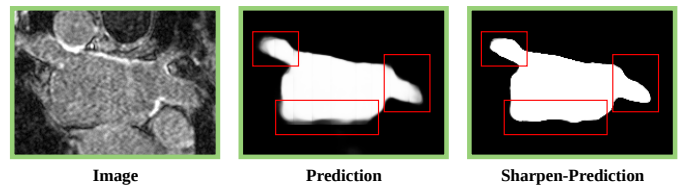


Fig. 3. Illustration of the results obtained from the sharpening operation. The red rectangles in the image highlight the regions where noticeable changes occurred before and after the sharpening process.

Subsequently, we employ the obtained soft-pseudo-labels $Pred_1^*$ and $Pred_2^*$ to supervise the probability maps $Pred_2$ and $Pred_1$ respectively, thereby enforcing the consistency constraint. This approach reduces the discrepancies between the decoder outputs and guides the model’s learning. Consequently, the consistency loss L_{con} for our model is defined as:

$$L_{con} = L_{mse}(Pred_1, Pred_1^*) + L_{mse}(Pred_2, Pred_2^*), \quad (11)$$

Where L_{mse} represents the mean squared error loss.

E. Loss Function

To further minimize the discrepancies between the decoder outputs, we compute the average of the probability maps $Pred_1$ and $Pred_2$ as the final output $Pred = \frac{1}{2} \cdot (Pred_1 + Pred_2)$ for the student model. Subsequently, we utilize $Pred$ to calculate the segmentation loss L_{seg} against the ground truth Y and the unsupervised segmentation loss L_{seg}^u against the pseudo-labels P obtained in the previous step. The overall loss is defined as:

$$L_{sup} = L_{dice}(Pred, Y) + L_{ce}(Pred, Y), \quad (12)$$

$$L_{unsup} = L_{dice}(Pred, P), \quad (13)$$

$$L_{total} = L_{sup} + L_{unsup} + \lambda L_{con}, \quad (14)$$

In the above equations, L_{ce} denotes the cross-entropy loss, L_{dice} represents the Dice loss [3]. The parameter λ represents a commonly employed time-dependent Gaussian warming-up function [5], utilized to modulate the equilibrium between the L_{con} loss and other relevant losses, which is defined as $\lambda(t) = w_{max} \cdot \exp(-5(1 - \frac{t}{t_{max}})^2)$, where w_{max} denotes the ultimate regularization weight, t signifies the current training step, and t_{max} represents the maximum training step. Specifically, L_{sup} is solely supervised with labeled data, L_{unsup} is solely supervised with mixed data, and L_{con} is supervised with all available data.

IV. EXPERIMENTS

A. Dataset and Preprocessing

To evaluate our approach, we conducted comprehensive evaluations on three publicly available medical image datasets, namely the Pancreas-CT dataset [37], the LA dataset [38], and the ACDC dataset [39].

1) *Pancreas-CT dataset*: The pancreas-CT dataset [37] used in this study was obtained from the National Institutes of Health Clinical Center. It consists of 82 3D abdominal contrast-enhanced CT scans acquired using Philips and Siemens MDCT scanners. The scans have a fixed in-plane resolution of 512×512 and varying intra-slice spacing ranging from 1.5 to 2.5 mm. The data split follows the same configuration as previous works [32], [34]. Specifically, 62 samples are used for model training, and the performance evaluation is conducted on the remaining 20 samples. To ensure appropriate

preprocessing, we applied a voxel value clipping operation based on [31], restricting the range to $[-125, 275]$ Hounsfield Units (HU). Subsequently, the data was further resampled to achieve an isotropic resolution of $1.0 \times 1.0 \times 1.0$ mm. Consistent with previous studies, our experiments encompassed three common semi-supervised settings, specifically training with 5% labeled data, training with 10% labeled data, and training with 20% labeled data. These settings allowed us to assess the model’s performance under varying degrees of labeled data availability.

2) *LA dataset*: The LA dataset [38], which serves as the benchmark dataset for the 2018 Atrial Segmentation Challenge, comprises 100 gadolinium-enhanced labeled MR scans with an isotropic resolution of $0.625 \times 0.625 \times 0.625$ mm. Since the annotations for the test set in LA are unavailable, we followed the established practice of using a fixed data split from previous studies. This split allocated 80 samples for training and reserved the remaining 20 samples for validation. In order to ensure a fair comparison with other models, we conducted performance comparisons using the same validation set. In line with previous research, our experiments encompassed three conventional semi-supervised settings: training with 5% labeled data, training with 10% labeled data, and training with 20% labeled data.

3) *ACDC dataset*: The ACDC (Automated Cardiac Diagnosis Challenge) dataset [39] was collected from real clinical exams conducted at the University Hospital of Dijon. This dataset consists of cardiac MR imaging samples obtained from 100 patients, specifically multi-slice 2-D cine MRI, which were used for training. Following the approach outlined in [31], we adopted a fixed data split at the patient level for our experiments, where the training, validation, and testing sets consisted of 70, 10, and 20 patients’ data, respectively. In contrast to the 3D binary segmentation tasks performed on the LA and Pancreas-CT datasets, we extended our model to address the 2D multi-class segmentation challenge presented by the ACDC dataset. Specifically, the 2D DCPA model was designed to segment three targets, including the myocardium, left ventricle, and right ventricle, from the 2D MR slices in this dataset. The same configurations, specifically training with 5% labeled data, 10% labeled data, and 20% labeled data, were employed in our experiments, consistent with the setups used for both the LA dataset and the Pancreas-CT dataset.

B. Implementation Details

1) *3D Segmentation*: In accordance with previous studies [28], [31], [34], preprocessing techniques were applied to the 3D scans, involving cropping based on ground truth annotations and normalization to achieve zero mean and unit variance prior to inputting them into the neural networks. Due to the computational demands associated with training 3D data, a patch-based approach was employed during the training phase, where the training data was divided into smaller patches. Specifically, for the LA dataset, the dimensions of the training patches were set to $112 \times 112 \times 80$, while for the pancreas-CT dataset, the patch size was defined as $96 \times 96 \times 96$. To augment the LA dataset, data augmentation techniques such as

2D rotation and flip operations were applied. For both datasets, a batch size of 4 was utilized, consisting of two labeled patches and two unlabeled patches. The V-Net architecture served as the underlying 3D backbone for our models. The 3D DCPA model was trained for a total of 15,000 iterations. During the inference stage, a patch-based pipeline employing a sliding window strategy was employed to combine the predictions from the patches and generate the final segmentation outputs.

2) *2D Segmentation*: On the ACDC dataset, we implemented normalization techniques to achieve a zero mean and unit variance for the samples. Additionally, data augmentation was performed by randomly applying rotations and flips to enhance the diversity of the dataset. From the ACDC dataset, we randomly extracted 2D patches with dimensions of 256×256 to create training samples. During the training phase, a batch size of 24 was used, consisting of 12 labeled data and 12 unlabeled samples. For testing, the scans were resized to 256×256 as inputs and subsequently enlarged to their original size to generate the final segmentation results. Our 2D DCPA model employed the U-Net architecture as its backbone. The model was trained for a total of 30,000 iterations to optimize its performance. It is worth noting that all experimental configurations on the ACDC dataset adhered to the guidelines set by the public benchmark established by [40], ensuring fairness and accuracy in the comparisons with other methods.

3) *Experimental settings*: All experiments were conducted on a server equipped with an NVIDIA GeForce RTX 3090 24GB GPU running Ubuntu 20.04 and PyTorch 1.12.1. To optimize the segmentation tasks, we employed an SGD optimizer with a momentum of 0.9 and weight decay of 0.0001. The initial learning rate was set to 0.01. Regarding the hyperparameter settings, K was defined as 2, T was set to 0.1, H was established as 0.5, and α was assigned a value of 0.75 for all tasks. Please note that we refrain from employing morphological operations to enhance the segmented outcomes, such as opting for the largest connected component as the post-processing module [30], [40]. In the context of comparative experiments, we utilized four metrics for evaluation: Dice, Jaccard, the 95% Hausdorff Distance (95HD), and average surface distance (ASD).

C. Experimental comparisons across different datasets

In order to assess the effectiveness of our proposed method, we conducted a series of comparative experiments involving several supervised and semi-supervised techniques, including V-Net [3], UA-MT [28], SASSNet [30], DTC [31], URPC [32], SS-Net [40], and MC-Net+ [34]. These methods were evaluated on three commonly employed publicly available datasets: Pancreas-CT dataset [37], LA dataset [38], and ACDC dataset [39]. The experiments were conducted in three settings, where 5%, 10% and 20% of the training images were annotated, respectively. The ensuing results obtained from the comparative analysis across the different datasets are presented below.

1) *Results on the Pancreas-CT dataset*: Table. I presents a quantitative comparison between our model and six distinct semi-supervised methodologies on the Pancreas-CT dataset.

Additionally, it includes the results obtained from training the V-Net model with 5%, 10%, 20%, and all labeled data for comprehensive supervision. The outcomes clearly demonstrate that our model has achieved substantial enhancements in performance when contrasted with the preceding models. Particularly noteworthy is the enhancement achieved under the scenario of 5% labeled data, where our method elevates the Dice score from 29.32% to 79.16% and markedly reduces the 95HD from 43.67 to 5.88. Under 10% labeled data, in comparison to the SOTA URPC model, our method raises the Dice score from 73.53% to 81.34%, while also diminishing the 95HD from 22.57 to 5.40. It is important to highlight that our method, leveraging merely 5% labeled data, manages to attain metrics that are akin to those of other semi-supervised approaches employing 20% labeled data. Additionally, with only 10% labeled data, our method outperforms other semi-supervised techniques that rely on 20% labeled data. Similarly, under 20% labeled data, our method attains a Dice score of 82.89%, nearing the performance of 83.48% Dice score achieved with 100% labeled data under supervised learning. The outcomes underscore our model’s capacity to attain high-quality performance on the challenging Pancreas-CT dataset, even when confronted with a restricted quantity of annotated data. This serves to establish the effectiveness of our approach.

Fig. 4 showcases the visualized segmentation outcomes achieved through training with 5% and 10% annotated data on the Pancreas-CT dataset, presented from both 2D and 3D perspectives. It is readily apparent that our model yields results that exhibit a closer alignment with the ground truth when compared to other state-of-the-art (SOTA) methods. In the 2D view, our model establishes clearer boundaries, effectively mitigating false positives and false negatives in contrast to alternative methodologies. The 3D view, as indicated by the green arrows, emphasizes regions where substantial deviations between our model and the ground truth exist. Notably, in the 3D visualization trained with 5% annotated data, competing methods not only fall short in achieving a comprehensive pancreas segmentation but also demonstrate a substantial occurrence of false positives. In stark contrast, our method delivers results that closely approximate the ground truth.

2) *Results on the LA dataset*: Table. II presents the quantitative results obtained for the LA dataset. Our proposed DCPA model demonstrates remarkable performance in training scenarios with 5%, 10% and 20% annotated data, effectively leveraging the potential of unlabeled data. In the context of training with a mere 5% of annotated data, the DCPA model emerges as a superior contender when compared to the fully supervised V-Net model. This accomplishment is accentuated by a noteworthy surge in the Dice coefficient, elevating impressively from 52.55% to 89.34%. Simultaneously, in contrast to the previous SOTA model, SS-Net, which trains within the confines of 5% annotated data, our proposed model demonstrates a significant advancement. This is evidenced by the Dice coefficient’s escalation from 86.33% to 89.34%, accompanied by a reduction in the 95HD from 9.97 to 8.13. It is of particular significance to emphasize that the performance metrics achieved by our DCPA model, trained exclusively on 5% annotated data, outperform those achieved by other semi-

TABLE I
COMPARISON WITH SOTA METHODS ON THE PANCREAS-CT DATASET.

Method	Scans used		Metrics			
	Labeled	Unlabeled	Dice(%) \uparrow	Jaccard(%) \uparrow	95HD(voxel) \downarrow	ASD(voxel) \downarrow
V-Net	3(5%)	0	29.32	19.61	43.67	15.42
V-Net	6(10%)	0	54.94	40.87	47.48	17.43
V-Net	12(20%)	0	71.52	57.68	18.12	5.41
V-Net	62(All)	0	83.48	71.99	4.44	1.26
UA-MT (MICCAI'19)			43.15	29.07	51.96	20.00
SASSNet (MICCAI'20)			41.48	27.98	47.48	18.36
DTC (AAAI'21)			47.57	33.41	44.17	15.31
URPC (MIA'22)	3(5%)	59(95%)	45.94	34.14	48.80	23.03
SS-Net (MICCAI'22)			41.39	27.65	52.12	19.37
MC-Net+ (MIA'22)			32.45	21.22	58.57	24.84
Ours			79.16	65.86	5.88	1.69
UA-MT (MICCAI'19)			66.44	52.02	17.04	3.03
SASSNet (MICCAI'20)			68.97	54.29	18.83	1.96
DTC (AAAI'21)			66.58	51.79	15.46	4.16
URPC (MIA'22)	6(10%)	56(90%)	73.53	59.44	22.57	7.85
SS-Net (MICCAI'22)			73.44	58.82	12.56	2.91
MC-Net+ (MIA'22)			70.00	55.66	16.03	3.87
Ours			81.34	68.97	5.40	1.69
UA-MT (MICCAI'19)			76.10	62.62	10.84	2.43
SASSNet (MICCAI'19)			76.39	63.17	11.06	1.42
DTC (AAAI'21)			76.27	62.82	8.70	2.20
URPC (MIA'22)	12(20%)	50(80%)	80.02	67.30	8.51	1.98
SS-Net (MICCAI'22)			78.68	65.96	9.74	1.91
MC-Net+ (MIA'22)			79.37	66.83	8.52	2.03
Ours			82.89	71.17	4.54	1.23

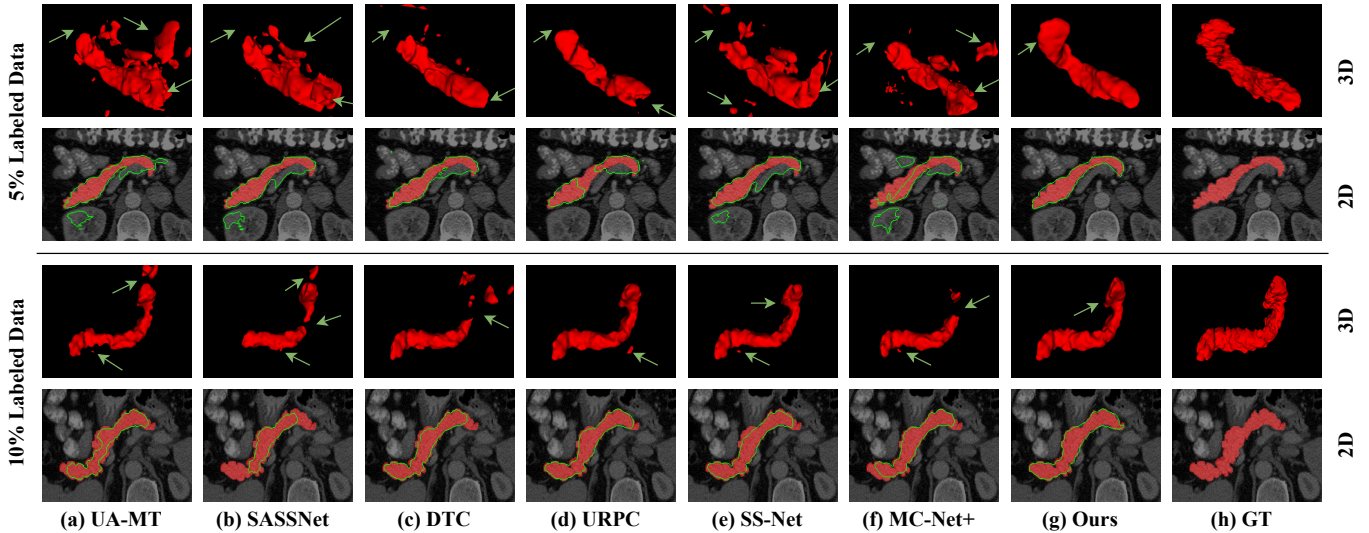


Fig. 4. Visualization of the 3D and 2D segmentation results obtained from various methods on the Pancreas-CT dataset. In the 2D segmentation visualization, the red regions correspond to the ground truth, while the green lines depict the corresponding predictions. For the 3D segmentation visualization, the predictions are represented by the red 3D volume.

supervised methods employing 10% annotated data. Moreover, in scenarios involving training with 10% annotated data, our model excels beyond the majority of semi-supervised segmentation models trained with 20% annotated data. Moreover, the DCPA model trained with only 20% annotated data achieves equivalent performance compared to the V-Net model trained with 100% annotated data. For instance, the Dice coefficients are 91.64% and 91.71%, the HD95 values are 5.04 and 5.57,

and the ASD values are 1.52 and 1.59, respectively. This finding suggests that our DCPA model effectively preserves fine details in the segmentation, reflected in the superior HD95 and ASD values, despite a minor change in the overall Dice coefficient. These results emphasize the robustness segmentation capabilities of our proposed method in the context of the LA dataset.

Fig. 5 depicts the segmentation outcomes of two samples

TABLE II
COMPARISON WITH SOTA METHODS ON THE LA DATASET.

Method	Scans used		Metrics			
	Labeled	Unlabeled	Dice(%) \uparrow	Jaccard(%) \uparrow	95HD(voxel) \downarrow	ASD(voxel) \downarrow
V-Net	4(5%)	0	52.55	39.60	47.05	9.87
V-Net	8(10%)	0	78.57	66.96	21.20	6.07
V-Net	16(20%)	0	86.96	77.31	11.85	3.22
V-Net	80(All)	0	91.71	84.76	5.57	1.59
UA-MT (MICCAI'19)			82.26	70.98	13.71	3.82
SASSNet (MICCAI'19)			81.60	69.63	16.60	3.58
DTC (AAAI'21)			81.25	69.33	14.90	3.99
URPC (MIA'22)	4(5%)	76(95%)	82.48	71.35	14.65	3.65
SS-Net (MICCAI'22)			86.33	76.15	9.97	2.31
MC-Net+ (MIA'22)			82.07	70.38	20.49	5.72
Ours			89.34	80.79	8.13	1.69
UA-MT (MICCAI'19)			86.28	76.11	18.71	4.63
SASSNet (MICCAI'19)			85.22	75.09	11.18	2.89
DTC (AAAI'21)			87.51	78.17	8.23	2.36
URPC (MIA'22)	8(10%)	72(90%)	85.01	74.36	15.37	3.96
SS-Net (MICCAI'22)			88.43	79.43	7.95	2.55
MC-Net+ (MIA'22)			88.96	80.25	7.93	1.86
Ours			90.91	83.39	5.53	1.65
UA-MT (MICCAI'19)			88.74	79.94	8.39	2.32
SASSNet (MICCAI'19)			89.16	80.60	8.95	2.26
DTC (AAAI'21)			89.52	81.22	7.07	1.96
URPC (MIA'22)	16(20%)	64(80%)	88.74	79.93	12.73	3.66
SS-Net (MICCAI'22)			89.86	81.70	7.01	1.87
MC-Net+ (MIA'22)			91.07	83.67	5.84	1.99

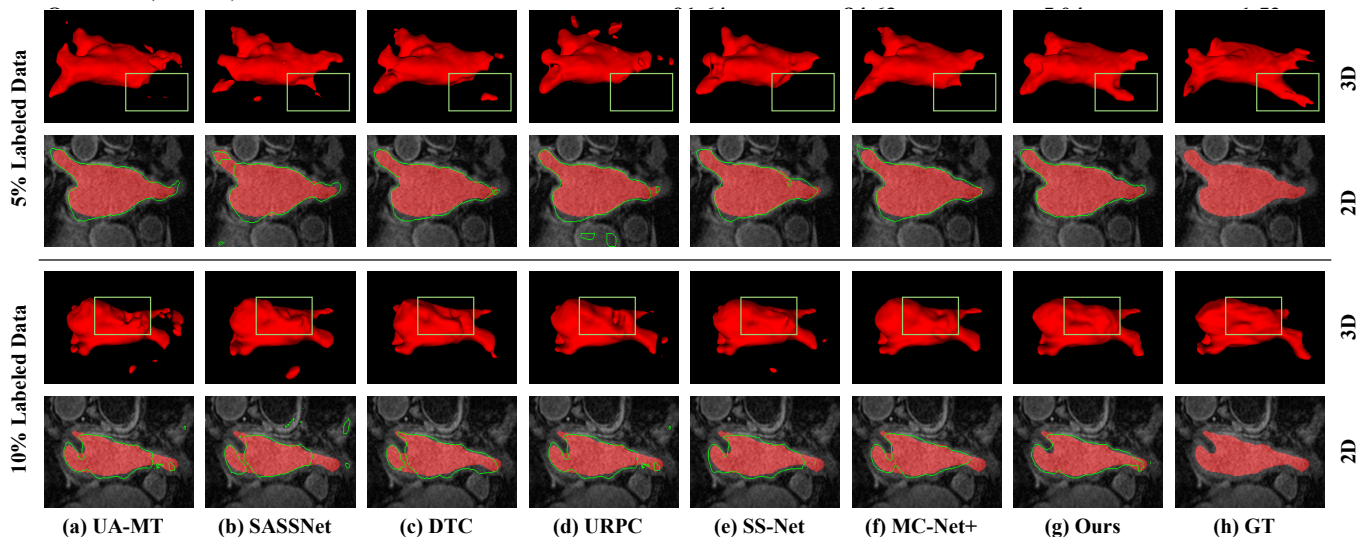


Fig. 5. Visualization of the 3D and 2D segmentation results obtained from various methods on the LA dataset. In the 2D segmentation visualization, the red regions correspond to the ground truth, while the green lines depict the corresponding predictions. For the 3D segmentation visualization, the predictions are represented by the red 3D volume.

extracted from the LA dataset, visualized from both 2D and 3D perspectives. The presented results are generated using five state-of-the-art (SOTA) models in conjunction with our proposed DCPA method, arranged sequentially from left to right. These findings conspicuously illustrate the superiority of the DCPA model in achieving a more comprehensive segmentation of the left atrium in comparison to the other SOTA methodologies. Furthermore, in the 3D view, our results exhibit a closer proximity to the ground truth, particularly within the regions delineated by the green rectangular boxes, where our algorithm surpasses the comparative methods. This

emphasizes the heightened accuracy of our approach. Consequently, the DCPA model effectively addresses the challenge posed by isolated regions and retains finer anatomical details, culminating in an overarching enhancement in the quality of semi-supervised left atrium segmentation.

3) *Results on the ACDC dataset:* We have further extended the application of DCPA to two-dimensional multi-class segmentation tasks. Table. III presents a comparative analysis of our results with the latest research findings from the ACDC dataset. The values presented in Table. III represent the averaged performance metrics for three segmented structures:

TABLE III
COMPARISON WITH SOTA METHODS ON THE ACDC DATASET.

Method	Scans used		Metrics			
	Labeled	Unlabeled	Dice(%) \uparrow	Jaccard(%) \uparrow	95HD(voxel) \downarrow	ASD(voxel) \downarrow
UNet	3(5%)	0	47.83	37.01	31.16	12.62
UNet	7(10%)	0	77.34	66.20	9.18	2.45
UNet	14(20%)	0	85.15	75.48	6.20	2.12
UNet	70(All)	0	91.65	84.93	1.89	0.56
UA-MT (MICCAI'19)			50.04	39.57	29.31	9.88
SASSNet (MICCAI'19)			57.77	46.14	20.05	6.06
DTC (AAAI'21)			56.90	45.67	23.36	7.39
URPC (MIA'22)	3(5%)	67(95%)	55.87	44.64	13.60	3.74
SS-Net (MICCAI'22)			65.82	55.38	6.67	2.28
MC-Net+ (MIA'22)			64.77	54.06	12.39	3.45
Ours			85.86	76.13	5.83	2.03
UA-MT (MICCAI'19)			81.58	70.48	12.35	3.62
SASSNet (MICCAI'19)			84.14	74.09	5.03	1.40
DTC (AAAI'21)			82.71	72.14	11.35	2.99
URPC (MIA'22)	7(10%)	63(90%)	81.77	70.85	5.04	1.41
SS-Net (MICCAI'22)			86.78	77.67	6.07	1.40
MC-Net+ (MIA'22)			87.10	78.06	6.68	2.00
Ours			88.10	79.45	1.86	0.57
UA-MT (MICCAI'19)			85.87	76.78	5.06	1.54
SASSNet (MICCAI'19)			87.04	78.13	7.84	2.15
DTC (AAAI'21)			86.28	77.03	6.14	2.11
URPC (MIA'22)	14(20%)	56(80%)	85.07	75.61	6.26	1.77
SS-Net (MICCAI'22)			88.10	79.70	3.34	0.95
MC-Net+ (MIA'22)			88.51	80.19	5.35	1.54
Ours			89.19	81.08	1.71	0.46

the myocardium, left ventricle, and right ventricle on the ACDC dataset. The results indicate that amidst a spectrum of semi-supervised scenarios, our model attains leading positions across Dice, Jaccard, 95HD, and ASD metrics, outshining competing approaches. Significantly, through the utilization of a mere 5% of labeled data, our model achieves an impressive Dice score of 85.86%, signifying a notable distinction from the U-Net model's score of 47.83%. In parallel, in comparison to the previous state-of-the-art model, SS-Net, our approach showcases a substantial enhancement in the Dice score, progressing from 65.82% to 85.86%. This significant improvement in performance helps demonstrate the exceptional capability of our proposed methodology. Irrespective of the assigned values of labeled data, our model consistently maintains a Dice score exceeding 85.00%, thereby demonstrating the robustness of the model.

Fig. 6 presents a visual comparative analysis of diverse methodologies trained on the ACDC dataset, utilizing a mere 5% of annotated data. Within this visualization, the left ventricle, myocardium, and right ventricle are delineated by the distinct hues of red, green, and blue, respectively. The visual interpretation unequivocally reveals that, when confronted with the intricate task of segmenting the left ventricle, the majority of methodologies yield suboptimal segmentation outcomes. Similarly, the task of demarcating clear boundaries for the myocardium and right ventricle proves to be a formidable challenge for a significant portion of the evaluated methods. In striking contrast, our proposed approach attains segmentation performance that remarkably aligns with the ground truth. This visual outcome serves to accentuate the robust and compelling

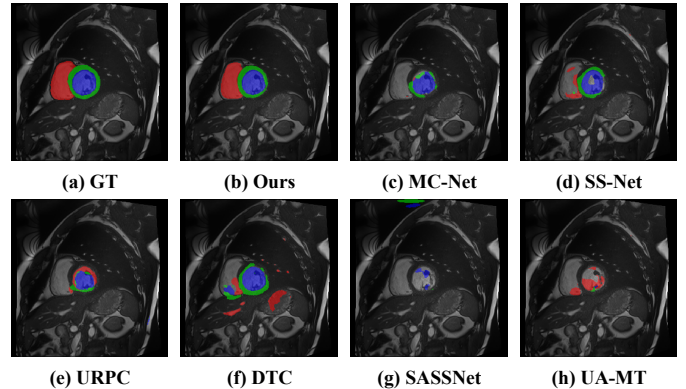


Fig. 6. The visual comparative results between our proposed method and the current SOTA approach are showcased using the ACDC dataset with a 5% ratio of labeled data. The left ventricle, myocardium, and right ventricle are represented in red, green, and blue, respectively.

performance demonstrated by our introduced methodology.

V. DISCUSSION

A. Ablation Studies

In this section, we conducted a comprehensive ablation study to analyze the following aspects: 1) the effectiveness of each component of DCPA, 2) the effectiveness of the number of decoders n , 3) the effectiveness of the amount of weak data augmentation on unlabeled data K , and 4) the effectiveness of temperature T .

1) *Effectiveness of each component of DCPA:* We conducted ablation experiments employing the V-Net as the

TABLE IV
 ABLATION RESULTS WERE CONDUCTED ON EACH COMPONENT OF OUR DCPA MODEL USING THE PANCREAS-CT DATASET. IN THE CONTEXT OF THE ABLATION STUDY, "DD" INDICATES THE INCORPORATION OF DUAL-DECODER CONSISTENCY, "PL" DENOTES THE UTILIZATION OF PSEUDO-LABELS, AND "MT" SIGNIFIES THE INTEGRATION OF THE MEAN-TEACHER MODEL.

Scans used		Method				Metrics			
labeled	unlabeled	DD	PL	MT	Mixup	Dice(%) \uparrow	Jaccard(%) \uparrow	95HD(voxel) \downarrow	ASD(voxel) \downarrow
3(5%)	59(95%)					29.32	19.61	43.67	15.42
		✓				36.77	24.47	46.34	16.41
		✓	✓			44.55	30.55	55.97	21.20
		✓	✓	✓		62.65	47.59	34.57	12.08
		✓	✓	✓	✓	69.07	53.64	26.08	7.55
		✓	✓	✓	✓	79.16	65.86	5.88	1.69
6(10%)	56(90%)					54.94	40.87	47.48	17.43
		✓				66.56	52.10	16.80	2.32
		✓	✓			71.12	56.41	37.71	11.52
		✓	✓	✓		79.38	66.47	6.83	1.73
		✓	✓	✓	✓	78.02	64.44	9.61	3.02
		✓	✓	✓	✓	81.34	68.97	5.40	1.69
12(20%)	50(80%)					71.52	57.68	18.12	5.41
		✓				76.74	63.64	9.52	2.58
		✓	✓			79.17	66.23	9.79	2.56
		✓	✓	✓		81.38	69.04	8.71	3.71
		✓	✓	✓	✓	82.64	70.75	5.31	1.34
		✓	✓	✓	✓	82.89	71.17	4.54	1.23

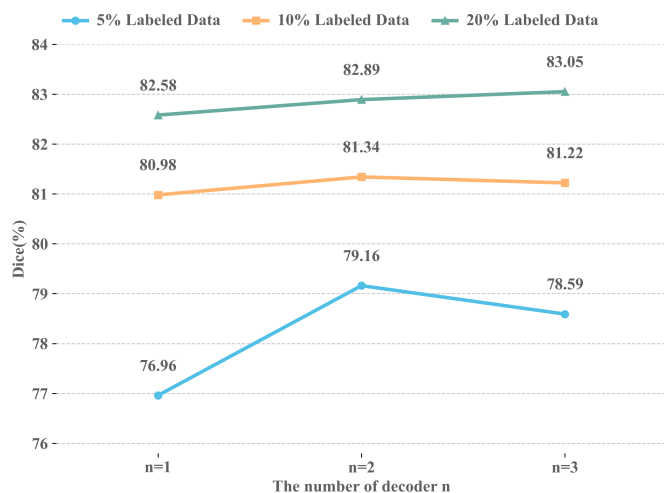


Fig. 7. Dice score variation based on the number of decoders in the Pancreas-CT dataset.

foundational model on the Pancreas-CT dataset across three distinct semi-supervised configurations. The purpose was to elucidate the effectiveness of each constituent component. The outcomes of these ablation experiments are meticulously documented in Table. IV. Embedded within the ablation study’s framework, the nomenclature "DD" signifies the incorporation of dual-decoder consistency, "PL" denotes the utilization of pseudo-labels, and "MT" conveys the integration of the mean-teacher model. The empirical findings compellingly underscore that within the realm of semi-supervised learning, each isolated constituent contributes discernibly to the accrual of performance gains. Moreover, the zenith of performance enhancement is achieved when these components synergistically combine.

2) *Effectiveness of the number of decoders n*: On the Pancreas-CT dataset, we conducted experiments under three semi-supervised settings to investigate the impact of the decoder quantity n on the experimental outcomes. The results of these experiments are illustrated in Fig. 7. In the experiments, when $n=1$, the utilization of the transposed convolutional layer for upsampling was employed. Correspondingly, $n=2$ introduced a second decoder incorporating the linear interpolation layer as the chosen upsampling strategy. Similarly to MC-Net+, for $n=3$, a third decoder with the nearest interpolation layer as the upsampling strategy is added. Notably, consistency losses between different decoders were incorporated for $n=2$ and $n=3$. The experimental findings demonstrate that augmenting the consistency loss with the decoder quantity can enhance performance. While $n=3$ achieves the highest performance of 83.05% with 20% labeled data training, it performs less effectively under the other two scenarios with fewer annotations. Moreover, it introduces higher training costs. Consequently, we ultimately select $n=2$ as the decoder quantity for our model.

3) *Effectiveness of the amount of weak data augmentation on unlabeled data K*: We conducted experiments on the Pancreas-CT dataset in three semi-supervised settings to investigate the impact of varying the value of K , which represents the number of times weak data augmentation is applied to unlabeled data. When K is set to 1, we directly use the predictions of the teacher model as pseudo-labels for unlabeled data. When K is not equal to 1, we use the average of the teacher model’s predictions as pseudo-labels for unlabeled data. The experimental results, as shown in Figure 8, indicate that under the 5% labeled data setting, the model’s performance fluctuates more significantly with changes in K . However, as the amount of labeled data increases, the impact of varying K on model performance becomes smaller. Notably, when K is set to 2, the best performance is consistently achieved across all

semi-supervised settings. Therefore, we adopt $K=2$ as the configuration for training our network.

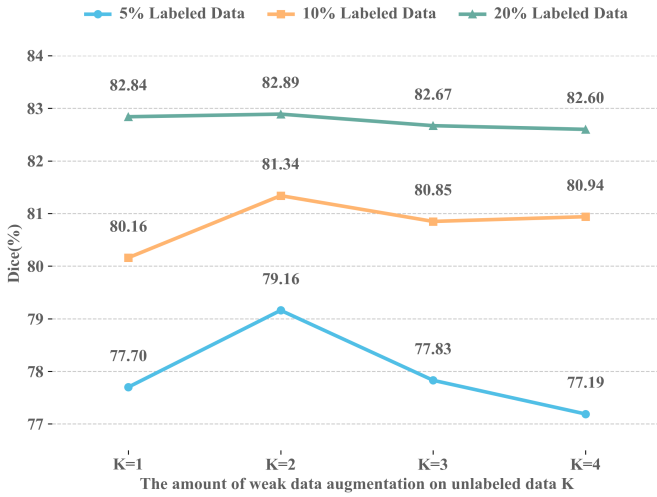


Fig. 8. Variability of dice score with respect to weak data augmentation levels on unlabeled data in the Pancreas-CT dataset.

4) *Effectiveness of sharpening temperatures T* : To mitigate blurry features and enhance segmentation boundary details, we introduce a sharpening function to apply entropy minimization constraints. We conducted experiments on three datasets with 10% labeled data to investigate the impact of the sharpening function’s temperature coefficient, denoted as T , on performance. The experimental outcomes are depicted in Fig. 9. The results highlight that our model exhibits a low sensitivity to variations in hyperparameters, indicating its robustness in handling such changes. Notably, we observe that the best performance is achieved when $T=0.1$. When the value of T becomes excessively large, the model becomes susceptible to the influence of blurry features, leading to relatively weaker performance. Conversely, when T is too small, the model is susceptible to the influence of erroneous predictions. Consequently, we select $T=0.1$ as the optimal choice for the temperature coefficient of the model’s sharpening function.

B. Limitations and Future Works

While the proposed DCPA method has achieved success in semi-supervised medical image segmentation, the introduction of the dual-decoder consistency approach has focused primarily on exploring the differences between decoders, and the range of available upsampling strategies is currently limited. Moving forward, our research presents several promising avenues for exploration. Firstly, we could delve into investigating the disparities between different models, such as contrasting Transformers and CNNs, to potentially leverage the strengths of each architecture. Secondly, exploring the synergies between our proposed Pseudo-Label Guided Data Augmentation method and other techniques like GANs [41] and Meta-Learning [42] could offer avenues for improved performance and robustness. Lastly, extending the applicability of our approach to broader medical image domains, exemplified by semi-supervised medical image classification, offers an avenue

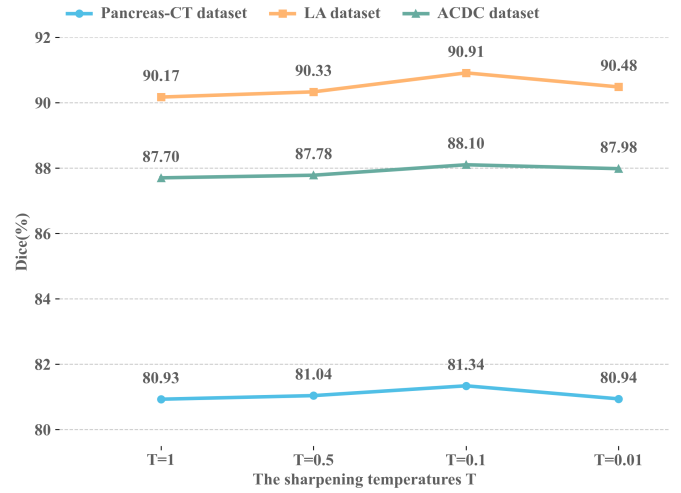


Fig. 9. The Dice scores were evaluated across three datasets under different sharpening temperatures T .

to harness the inherent potency of limited labeled data in the discrimination of benign and malignant cases.

VI. CONCLUSION

In this study, we have introduced a novel DCPA model for semi-supervised medical image segmentation. Firstly, leveraging the mean-teacher framework, we proposed a dual-decoder architecture, utilizing predictions from the teacher model as pseudo-labels for unlabeled data, which were employed to compute unsupervised loss. Secondly, a data augmentation strategy was employed by blending unlabeled data with labeled data. Furthermore, during the training of the student model, we imposed constraints on the disparities between the two decoders to compel the model to generate consistent predictions. Experimental outcomes have demonstrated that our model outperforms six state-of-the-art models across three semi-supervised settings on three publicly available medical datasets. Particularly noteworthy is our model’s exceptional performance under the 5% labeled data setting, which highlights its efficacy, robustness, and potential for conducting semi-supervised medical image segmentation with extremely limited data. This work not only establishes the effectiveness of our model but also paves the way for new frontiers in the realm of semi-supervised medical image segmentation.

REFERENCES

- [1] J. Long, E. Shelhamer, and T. Darrell, “Fully convolutional networks for semantic segmentation,” in *Proceedings of the IEEE conference on computer vision and pattern recognition*, pp. 3431–3440, 2015.
- [2] O. Ronneberger, P. Fischer, and T. Brox, “U-net: Convolutional networks for biomedical image segmentation,” in *Medical Image Computing and Computer-Assisted Intervention—MICCAI 2015: 18th International Conference, Munich, Germany, October 5–9, 2015, Proceedings, Part III 18*, pp. 234–241, Springer, 2015.
- [3] F. Milletari, N. Navab, and S.-A. Ahmadi, “V-net: Fully convolutional neural networks for volumetric medical image segmentation,” in *2016 fourth international conference on 3D vision (3DV)*, pp. 565–571, Ieee, 2016.
- [4] C. You, Y. Zhou, R. Zhao, L. Staib, and J. S. Duncan, “Simcvd: Simple contrastive voxel-wise representation distillation for semi-supervised medical image segmentation,” *IEEE Transactions on Medical Imaging*, vol. 41, no. 9, pp. 2228–2237, 2022.

- [5] S. Laine and T. Aila, "Temporal ensembling for semi-supervised learning," *arXiv preprint arXiv:1610.02242*, 2016.
- [6] A. Tarvainen and H. Valpola, "Mean teachers are better role models: Weight-averaged consistency targets improve semi-supervised deep learning results," *Advances in neural information processing systems*, vol. 30, 2017.
- [7] M. Sajjadi, M. Javanmardi, and T. Tasdizen, "Regularization with stochastic transformations and perturbations for deep semi-supervised learning," *Advances in neural information processing systems*, vol. 29, 2016.
- [8] M. Abdar, F. Pourpanah, S. Hussain, D. Rezazadegan, L. Liu, M. Ghavamzadeh, P. Fieguth, X. Cao, A. Khosravi, U. R. Acharya, *et al.*, "A review of uncertainty quantification in deep learning: Techniques, applications and challenges," *Information Fusion*, vol. 76, pp. 243–297, 2021.
- [9] D. Berthelot, N. Carlini, I. Goodfellow, N. Papernot, A. Oliver, and C. A. Raffel, "Mixmatch: A holistic approach to semi-supervised learning," *Advances in neural information processing systems*, vol. 32, 2019.
- [10] J. Chen, Z. Yang, and D. Yang, "Mixtext: Linguistically-informed interpolation of hidden space for semi-supervised text classification," *arXiv preprint arXiv:2004.12239*, 2020.
- [11] D.-H. Lee *et al.*, "Pseudo-label: The simple and efficient semi-supervised learning method for deep neural networks," in *Workshop on challenges in representation learning, ICML*, vol. 3, p. 896, 2013.
- [12] M. N. Rizve, K. Duarte, Y. S. Rawat, and M. Shah, "In defense of pseudo-labeling: An uncertainty-aware pseudo-label selection framework for semi-supervised learning," *arXiv preprint arXiv:2101.06329*, 2021.
- [13] P. Cascante-Bonilla, F. Tan, Y. Qi, and V. Ordonez, "Curriculum labeling: Revisiting pseudo-labeling for semi-supervised learning," 2020.
- [14] H. Zhang, M. Cisse, Y. N. Dauphin, and D. Lopez-Paz, "mixup: Beyond empirical risk minimization," *arXiv preprint arXiv:1710.09412*, 2017.
- [15] F. Isensee, P. F. Jäger, S. A. Kohl, J. Petersen, and K. H. Maier-Hein, "Automated design of deep learning methods for biomedical image segmentation," *arXiv preprint arXiv:1904.08128*, 2019.
- [16] J. Xu, M. Li, and Z. Zhu, "Automatic data augmentation for 3d medical image segmentation," in *Medical Image Computing and Computer Assisted Intervention—MICCAI 2020: 23rd International Conference, Lima, Peru, October 4–8, 2020, Proceedings, Part I 23*, pp. 378–387, Springer, 2020.
- [17] S. Zhang, H. Fu, Y. Yan, Y. Zhang, Q. Wu, M. Yang, M. Tan, and Y. Xu, "Attention guided network for retinal image segmentation," in *Medical Image Computing and Computer Assisted Intervention—MICCAI 2019: 22nd International Conference, Shenzhen, China, October 13–17, 2019, Proceedings, Part I 22*, pp. 797–805, Springer, 2019.
- [18] X. Xiao, S. Lian, Z. Luo, and S. Li, "Weighted res-unet for high-quality retina vessel segmentation," in *2018 9th international conference on information technology in medicine and education (ITME)*, pp. 327–331, IEEE, 2018.
- [19] K. He, X. Zhang, S. Ren, and J. Sun, "Deep residual learning for image recognition," in *Proceedings of the IEEE conference on computer vision and pattern recognition*, pp. 770–778, 2016.
- [20] Z. Gu, J. Cheng, H. Fu, K. Zhou, H. Hao, Y. Zhao, T. Zhang, S. Gao, and J. Liu, "Ce-net: Context encoder network for 2d medical image segmentation," *IEEE transactions on medical imaging*, vol. 38, no. 10, pp. 2281–2292, 2019.
- [21] A. Vaswani, N. Shazeer, N. Parmar, J. Uszkoreit, L. Jones, A. N. Gomez, L. Kaiser, and I. Polosukhin, "Attention is all you need," *Advances in neural information processing systems*, vol. 30, 2017.
- [22] H. Cao, Y. Wang, J. Chen, D. Jiang, X. Zhang, Q. Tian, and M. Wang, "Swin-unet: Unet-like pure transformer for medical image segmentation," in *European conference on computer vision*, pp. 205–218, Springer, 2022.
- [23] Z. Liu, Y. Lin, Y. Cao, H. Hu, Y. Wei, Z. Zhang, S. Lin, and B. Guo, "Swin transformer: Hierarchical vision transformer using shifted windows," in *Proceedings of the IEEE/CVF international conference on computer vision*, pp. 10012–10022, 2021.
- [24] H. Kervadec, J. Bouchtiba, C. Desrosiers, E. Granger, J. Dolz, and I. B. Ayed, "Boundary loss for highly unbalanced segmentation," *Medical image analysis*, vol. 67, p. 101851, 2021.
- [25] O. Chapelle, B. Scholkopf, and A. Zien, "Semi-supervised learning (chapelle, o. *et al.*, eds.; 2006)[book reviews]," *IEEE Transactions on Neural Networks*, vol. 20, no. 3, pp. 542–542, 2009.
- [26] Y. Zhao, K. Lu, J. Xue, S. Wang, and J. Lu, "Semi-supervised medical image segmentation with voxel stability and reliability constraints," *IEEE Journal of Biomedical and Health Informatics*, 2023.
- [27] Y. Wang, G. Huang, S. Song, X. Pan, Y. Xia, and C. Wu, "Regularizing deep networks with semantic data augmentation," *IEEE Transactions on Pattern Analysis and Machine Intelligence*, vol. 44, no. 7, pp. 3733–3748, 2021.
- [28] L. Yu, S. Wang, X. Li, C.-W. Fu, and P.-A. Heng, "Uncertainty-aware self-ensembling model for semi-supervised 3d left atrium segmentation," in *Medical Image Computing and Computer Assisted Intervention—MICCAI 2019: 22nd International Conference, Shenzhen, China, October 13–17, 2019, Proceedings, Part II 22*, pp. 605–613, Springer, 2019.
- [29] X. Li, L. Yu, H. Chen, C.-W. Fu, L. Xing, and P.-A. Heng, "Transformation-consistent self-ensembling model for semisupervised medical image segmentation," *IEEE Transactions on Neural Networks and Learning Systems*, vol. 32, no. 2, pp. 523–534, 2020.
- [30] S. Li, C. Zhang, and X. He, "Shape-aware semi-supervised 3d semantic segmentation for medical images," in *Medical Image Computing and Computer Assisted Intervention—MICCAI 2020: 23rd International Conference, Lima, Peru, October 4–8, 2020, Proceedings, Part I 23*, pp. 552–561, Springer, 2020.
- [31] X. Luo, J. Chen, T. Song, and G. Wang, "Semi-supervised medical image segmentation through dual-task consistency," in *Proceedings of the AAAI Conference on Artificial Intelligence*, vol. 35, pp. 8801–8809, 2021.
- [32] X. Luo, G. Wang, W. Liao, J. Chen, T. Song, Y. Chen, S. Zhang, D. N. Metaxas, and S. Zhang, "Semi-supervised medical image segmentation via uncertainty rectified pyramid consistency," *Medical Image Analysis*, vol. 80, p. 102517, 2022.
- [33] W. Hang, W. Feng, S. Liang, L. Yu, Q. Wang, K.-S. Choi, and J. Qin, "Local and global structure-aware entropy regularized mean teacher model for 3d left atrium segmentation," in *Medical Image Computing and Computer Assisted Intervention—MICCAI 2020: 23rd International Conference, Lima, Peru, October 4–8, 2020, Proceedings, Part I 23*, pp. 562–571, Springer, 2020.
- [34] Y. Wu, Z. Ge, D. Zhang, M. Xu, L. Zhang, Y. Xia, and J. Cai, "Mutual consistency learning for semi-supervised medical image segmentation," *Medical Image Analysis*, vol. 81, p. 102530, 2022.
- [35] R. Wang, Y. Wu, H. Chen, L. Wang, and D. Meng, "Neighbor matching for semi-supervised learning," in *Medical Image Computing and Computer Assisted Intervention—MICCAI 2021: 24th International Conference, Strasbourg, France, September 27–October 1, 2021, Proceedings, Part II 24*, pp. 439–449, Springer, 2021.
- [36] C. Li, L. Dong, Q. Dou, F. Lin, K. Zhang, Z. Feng, W. Si, X. Deng, Z. Deng, and P.-A. Heng, "Self-ensembling co-training framework for semi-supervised covid-19 ct segmentation," *IEEE Journal of Biomedical and Health Informatics*, vol. 25, no. 11, pp. 4140–4151, 2021.
- [37] K. Clark, B. Vendt, K. Smith, J. Freymann, J. Kirby, P. Koppel, S. Moore, S. Phillips, D. Maffitt, M. Pringle, *et al.*, "The cancer imaging archive (tcia): maintaining and operating a public information repository," *Journal of digital imaging*, vol. 26, pp. 1045–1057, 2013.
- [38] Z. Xiong, Q. Xia, Z. Hu, N. Huang, C. Bian, Y. Zheng, S. Vesal, N. Ravikumar, A. Maier, X. Yang, *et al.*, "A global benchmark of algorithms for segmenting the left atrium from late gadolinium-enhanced cardiac magnetic resonance imaging," *Medical image analysis*, vol. 67, p. 101832, 2021.
- [39] O. Bernard, A. Lalonde, C. Zotti, F. Cervensky, X. Yang, P.-A. Heng, I. Cetin, K. Lekadir, O. Camara, M. A. G. Ballester, *et al.*, "Deep learning techniques for automatic mri cardiac multi-structures segmentation and diagnosis: is the problem solved?," *IEEE transactions on medical imaging*, vol. 37, no. 11, pp. 2514–2525, 2018.
- [40] Y. Wu, Z. Wu, Q. Wu, Z. Ge, and J. Cai, "Exploring smoothness and class-separation for semi-supervised medical image segmentation," in *International Conference on Medical Image Computing and Computer Assisted Intervention*, pp. 34–43, Springer, 2022.
- [41] I. Goodfellow, J. Pouget-Abadie, M. Mirza, B. Xu, D. Warde-Farley, S. Ozair, A. Courville, and Y. Bengio, "Generative adversarial nets," *Advances in neural information processing systems*, vol. 27, 2014.
- [42] M. Ren, E. Triantafillou, S. Ravi, J. Snell, K. Swersky, J. B. Tenenbaum, H. Larochelle, and R. S. Zemel, "Meta-learning for semi-supervised few-shot classification," *arXiv preprint arXiv:1803.00676*, 2018.